

Layer-Dependent Photoabsorption and Photovoltaic Effects in Two-Dimensional Bi₂O₂X (X = S, Se, and Te)

Hao Tang^{1,†}, Bowen Shi^{1,†}, Yangyang Wang², Chen Yang¹, Shiqi Liu¹, Ying Li,¹
Ruge Quhe,³ and Jing Lu^{1,4,5,6,*}

¹State Key Laboratory for Mesoscopic Physics and Department of Physics, Peking University, Beijing 100871, People's Republic of China

²Nanophotonics and Optoelectronics Research Center, Qian Xuesen Laboratory of Space Technology, China Academy of Space Technology, Beijing 100094, People's Republic of China

³State Key Laboratory of Information Photonics and Optical Communications and School of Science, Beijing University of Posts and Telecommunications, Beijing 100876, People's Republic of China

⁴Collaborative Innovation Center of Quantum Matter, Beijing 100871, People's Republic of China

⁵Beijing Key Laboratory for Magnetolectric Materials and Devices (BKL-MEMD), Beijing 100871, People's Republic of China

⁶Key Laboratory for the Physics and Chemistry of Nanodevices, Peking University, Beijing 100871, People's Republic of China

(Received 21 December 2020; revised 25 March 2021; accepted 20 May 2021; published 15 June 2021)

Significant photoconductive effects are reported in emergent two-dimensional (2D) Bi₂O₂Se. In this work, we investigate the layer-dependent photoresponse properties and photovoltaic effects of 2D Bi₂O₂X ($X = S$, Se, and Te) by first-principles calculations and quantum-transport simulation. The absorbance per layer increases with the decreasing layer number for high-frequency light, so the absorbance density of 2D Bi₂O₂X can be elevated by decreasing the layer number. An outstanding open-circuit voltage (1.08 V) among 2D materials is found for the monolayer (ML) Bi₂O₂Se *p-n* junction. The computed responsivities of ML black phosphorous, MoS₂, and WSe₂ *p-n* junctions through our methods are in good agreement with experiments. The ML Bi₂O₂Se and Bi₂O₂Te *p-n* junctions show responsivities of 16.8 and 13.6 mA/W, respectively, under AM1.5 sunlight; these values are higher than those of their extensively studied ML MoS₂ (8.6) and WSe₂ (8.8) counterparts. The Bi₂O₂Se film and Bi₂O₂S *p-n* junctions also show higher responsivities than those of commercial Si and GaAs. Therefore, the 2D Bi₂O₂X *p-n* junctions have prospective applications in photovoltaic devices.

DOI: 10.1103/PhysRevApplied.15.064037

I. INTRODUCTION

Two-dimensional (2D) materials are promising materials for photovoltaic and photoelectronic applications [1–3] because of their strong interaction with light [4], variety of band gaps, good carrier transportation [5,6], easy construction of van der Waals heterostructures, easy modulation by an electrical field, and depressed dark currents [7]. The absorption coefficients of typical 2D materials [graphene and transition-metal dichalcogenides (TMDs)] are one order of magnitude higher than those of common photoelectronic bulk materials (Si and GaAs) [8]. For example, the absorbance of a visible photon with an energy of 1–2.5 eV by monolayer (ML) MoS₂ reaches

5%–10% [8], which is equivalent to approximately 50-nm-thick Si [9]. Despite the limited total light absorbance of the few-layer material, it can produce extraordinarily high power density in devices. The power densities of graphene/MoS₂ and WS₂/MoS₂ solar cells are predicted to be in the range of 1000–10 000 and 3000–12 000 kW/L, respectively; these values are much higher than those of 5.9 and 290 kW/L recorded in in Si and GaAs ultrathin solar cells, respectively [8].

2D Bi₂O₂X ($X = S$, Se, and Te) layered materials, where X^{2-} ions intercalate between stacked covalently bonded [Bi₂O₂]²⁺ layers [10], are reported as a promising group of 2D materials for applications in electronics [11–13], thermoelectric [14–16], and photoelectronic devices [1,17]. Ionic bonding between the layers in Bi₂O₂X is different from the interlayer van der Waals interactions of most 2D materials, leading to unique stacking properties [18]. Recently, 2D Bi₂O₂Se has attracted intense

*jinglu@pku.edu.cn

†H. Tang and B. Shi contributed equally to this work.

research interest due to its moderate band gap (0.8–1.3 eV from bulk to ML) [11], reasonably high carrier mobility ($450 \text{ cm}^2 \text{ V}^{-1} \text{ s}^{-1}$ at 300 K and $3 \times 10^5 \text{ cm}^2 \text{ V}^{-1} \text{ s}^{-1}$ at 2 K) [11,18], good air stability [18], and excellent device performance at the sub-10-nm region [12,13]. Experimental methods are developed to grow millimeter-sized 2D $\text{Bi}_2\text{O}_2\text{Se}$ films with accurate control of their thickness [19], enabling the fabrication of macroscopic scale devices [17]. Significant photoconductive effects are found in 2D $\text{Bi}_2\text{O}_2\text{Se}$. For example, a very high responsivity of $3.5 \times 10^4 \text{ A/W}$ and specific detectivity of $9.0 \times 10^{13} \text{ Jones}$ are reported in a 2D $\text{Bi}_2\text{O}_2\text{Se}$ phototransistor [1]. A $\text{Bi}_2\text{O}_2\text{S}$ nanocrystal is also reported to be an excellent photoelectric material [10].

However, the two key effects, the layer dependence of photoabsorption and photovoltaic effect, have not been investigated in 2D Bi_2O_2X . Although the layer-dependent electronic structure of 2D $\text{Bi}_2\text{O}_2\text{Se}$ is provided, the layer-dependent optical properties of 2D $\text{Bi}_2\text{O}_2\text{Se}$ have not been calculated. Compared with the photoconductivity-effect device, the photovoltaic effect device (*p-n* junction) not only works at zero bias, but can also be used as a light-emitting diode (LED) [20], for solar energy conversion [21], and in logic circuits [7,22].

In the first part of this work, we investigate the absorption coefficients of 2D Bi_2O_2X through time-dependent density-functional theory (TD DFT) calculations. We find apparent enhancement in the high-frequency light absorptions of 2D Bi_2O_2X , arising from their 2D nature, and the absorbance of each layer increases with a decreasing layer number. In the second part, we calculate the photocurrent in *p-n* junctions of ML Bi_2O_2X via DFT coupled with the nonequilibrium Green function (NEGF) method. The calculated responsivities of typical ML materials [MoS_2 , WSe_2 , and black phosphorous (BP)] based on this method are in good agreement with previous experiments [21,23,24]. A very high open-circuit voltage of 1.08 V is found in ML $\text{Bi}_2\text{O}_2\text{Se}$ *p-n* junctions, and the responsivities of ML $\text{Bi}_2\text{O}_2\text{Se}$ (16.8 mA/W) and $\text{Bi}_2\text{O}_2\text{Te}$ (13.6 mA/W) *p-n* junctions are higher than those of their TMD counterparts under AM1.5 sunlight. The $\text{Bi}_2\text{O}_2\text{Se}$ film and $\text{Bi}_2\text{O}_2\text{S}$ *p-n* junctions also show higher responsivities of 1.9 and 1.3 A/W under AM1.5, respectively, than those of their commercial Si (0.5 A/W) and GaAs (1.2 A/W) counterparts [22]. Our results indicate the promising application of 2D Bi_2O_2X *p-n* junctions in photovoltaic devices.

II. METHODS

The electronic ground states of bulk and 2D Bi_2O_2X are calculated by the hybrid functional method with the HSE06 functional [25]. The projector-augmented-wave (PAW) methods implemented in the Vienna *ab initio* simulation package (VASP) [26,27] are used for all calculations with a cutoff energy of 500 eV. The *k*-point meshes are

sampled by the Monkhorst-Pack scheme [28] with a separation of 0.2 \AA^{-1} . A vacuum layer of 10 Å is used for the 2D calculations, and dipole corrections are used to eliminate fake interactions. The DFT D3 method is used to consider the van der Waals interactions [29]. The energy in electronic iterations converges to 10^{-5} eV , and the residual force in the ionic relaxation converges to 0.02 eV/\AA per atom.

The optical properties are calculated through dielectric functions by both the single-particle approximation [30] and the Casida equation [31] after a ground-state HSE06 calculation. Six valence bands and 12 conduction bands are included in the Casida equation on a 9×9 *k*-points grid to derive the low-energy photon-absorption spectra. The method we adopt employs a hybrid XC kernel in the electron-hole ladder diagram in the Casida equation, considering a local exchange correlation and the exact exchange [31]. As TD DFT does not capture the long-range correlation, the exciton effects are not accurately included [32,33]. Generally, the state-of-art method for optical absorption is the GW + Bethe-Salpeter equation (BSE) scheme that accurately considers the exciton effects [34,35]. We examine the validity of TD DFT by comparing it with the absorbance of ML $\text{Bi}_2\text{O}_2\text{Se}$ calculated by GW BSE (see results), and the two results show reasonable consistency. So, the absorption spectra we derive here are approximately valid for Bi_2O_2X .

Lateral *p-n* junctions are constructed to simulate the Bi_2O_2X photodetection devices. The Perdew-Burke-Ernzerhof (PBE) functional with the generalized gradient approximation (GGA) is used to calculate the device ground states, and the transport properties are calculated at a temperature of 300 K. The periodic, Neuman, and Dirichlet boundary conditions are used in the *x*, *y*, and *z* directions, respectively. The GGA method is approximately valid here, as the central region of the devices is heavily doped, leading to a strong screening effect and reasonable prediction of the single-particle approximation. The photocurrent spectrum is calculated by the NEGF method, considering the single-photon-absorption process implemented in the Atomistix Toolkit 2018 package [36,37]:

$$I_\alpha = \frac{e}{\hbar} \int_{-\infty}^{+\infty} \sum_{\beta=L,R} [1 - f_\alpha(E)] f_\beta(E - \hbar\omega) T_{\alpha,\beta}^-(E) - f_\alpha(E) [1 - f_\beta(E + \hbar\omega)] T_{\alpha,\beta}^+(E) dE, \quad (1)$$

where $f_\alpha(E)$ is the Fermi distribution function of electrode α [both α and β go through *L* (left) and *R* (right)], e is the charge of an electron, and \hbar is the reduced Plank constant. The first term represents transport from electrode β to α , and the second term represents the opposite transport; both processes include single-photon absorption. $T_{\alpha,\beta}^\pm$ is the transmission coefficient with the absorption of a single

photon calculated by

$$\begin{aligned} T_{\alpha,\beta}^-(E) &= N \operatorname{Tr}[M^+ \tilde{A}_\alpha(E) M A_\beta(E - \hbar\omega)], N T_{\alpha,\beta}^+(E) \\ &= N \operatorname{Tr}[M \tilde{A}_\alpha(E) M^+ A_\beta(E + \hbar\omega)], \end{aligned} \quad (2)$$

where N and M are the numbers of photons and the transition matrix of the photon-absorption process, respectively. A_α is the spectral function defined as $A_\alpha = G\Gamma_\alpha G^+$, where G and Γ_α are the Green function and broadening function, respectively.

III. RESULTS AND DISCUSSION

A. Electronic and photoelectric properties of bulk and ML Bi₂O₂X

The Bi₂O₂X crystals consist of alternatively stacked [Bi₂O₂]²⁺ layers and X²⁻ ions, with I4/mmm space group symmetry, as shown in Fig. 1(a). The relaxed lattice parameters in our calculations are $a = b = 3.85, 3.91$, and 4.00 \AA , $c = 11.99, 12.23$, and 12.73 \AA for $X = \text{S}, \text{Se}$, and Te , respectively; these values are in good agreement with those obtained experimentally [1, 10, 38, 39]. The consistency with $c = 11.92, 12.16$, and 12.70 \AA in experiments confirms that our calculation properly considers interlayer interactions. We construct the 2D structures by separating the crystal in the c direction through the ionic bonds between [Bi₂O₂] layers and X²⁻ ions, as shown

in Fig. 1(b). However, the surface atomic configurations are not explicitly characterized in previous experiments. According to our calculations, the structure with Se atoms on both sides reproduces the experimental band gap, but the Fermi level is outside the band gap. We passivate both sides with hydrogen to obtain a semiconductor (Fig. S4 within the Supplemental Material [40]). The H-passivated configuration of 2D Bi₂O₂Se is used in DFT calculations to explain the band gap's layer dependence in experiments [18]. To examine the configuration's validity, we calculate the indirect band gap of ML H-passivated Bi₂O₂Se with the HSE06 functional to be 2.1 eV (see Fig. S2 within the Supplemental Material [40]), which is consistent with the indirect band gap of 1.95 eV determined by optical measurement [18]. Therefore, we expect that calculating such configurations could approximately simulate the electronic structure of 2D Bi₂O₂X under experimental conditions.

The HSE band structures of the Bi₂O₂X crystals are shown in Figs. 1(c)–1(e). The shapes of both the conduction bands and valence bands are similar in the three materials, while the band gaps are different for S, Se, and Te. Indirect band gaps from X [valence-band maximum (VBM)] to Γ [conduction-band minimum (CBM)] of 1.49, 0.95, and 0.25 eV are obtained for $X = \text{S}, \text{Se}$, and Te , respectively; these values are close to those previously reported [10, 41, 42]. Direct band gaps of 1.83, 1.60, and 1.19 eV are located at the Γ point for S, Se, and Te, respectively. The direct gaps of Bi₂O₂Se and Bi₂O₂Te are

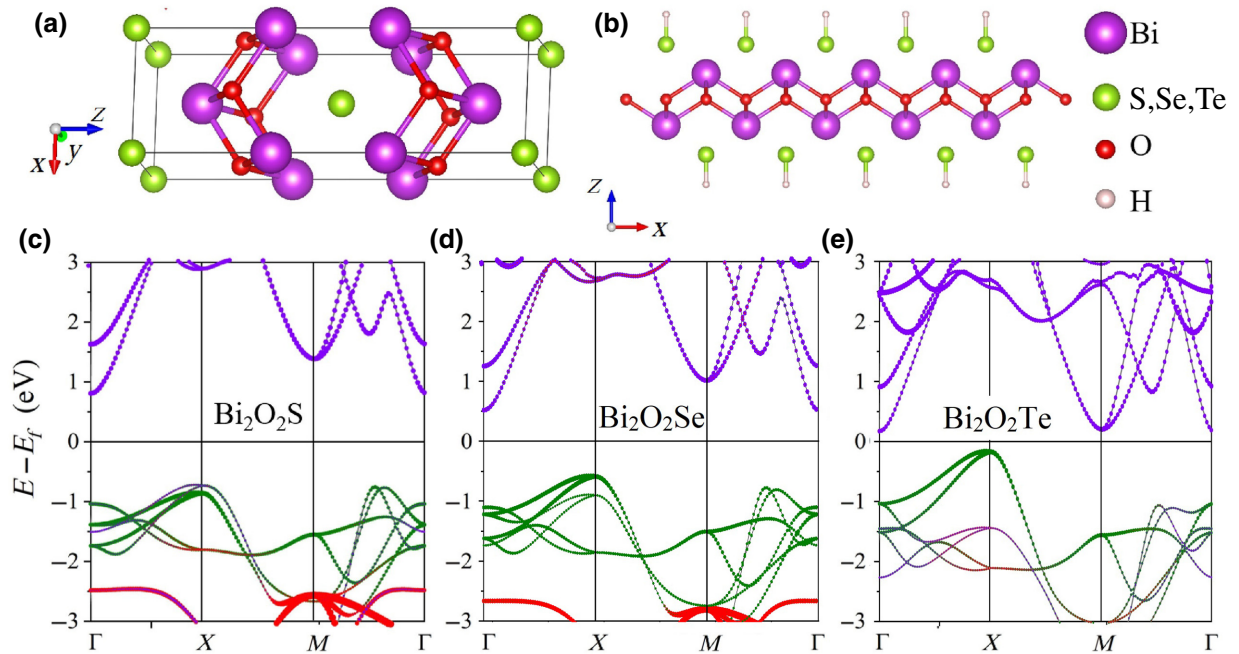


FIG. 1. Geometry and band structures of Bi₂O₂X. (a) Atomic structure of a single unit cell of bulk Bi₂O₂X crystal. (b) Side view of ML Bi₂O₂X passivated by hydrogen atoms. Purple, green, red, and white balls represent Bi; S, Se, or Te; O; and H atoms, respectively. (c)–(e) Projected band structures of Bi₂O₂S, Bi₂O₂Se, and Bi₂O₂Te, respectively, calculated with HSE06 functional. Green, purple, and red dots represent projection weights of S, Se, or Te; Bi; and O orbitals, respectively.

small enough to absorb the full spectrum of visible light through a direct transition.

The conduction-band states are dominated by the orbitals of Bi, while the valence-band states are dominated by the p_x and p_y orbitals of X^{2-} . The transition of electrons through the direct band gap at the Γ point is prohibited for the absorption of z -polarized incident photon due to inversion symmetry in the x - y direction. Therefore, the absorption of z -polarized light with a frequency corresponding to the direct band gap is significantly lower. Such properties provide the possibility for polarization detection of light over a specific frequency range.

We calculate the optical properties of bulk and 2D Bi_2O_2X through the Casida equation. Because of tetrahedral symmetry, the dielectric matrix ϵ_{ij} has a diagonal form and equivalence in the x and y directions:

$$\epsilon = \begin{pmatrix} \epsilon_{xx} & 0 & 0 \\ 0 & \epsilon_{xx} & 0 \\ 0 & 0 & \epsilon_{zz} \end{pmatrix}. \quad (3)$$

The absorption coefficient α of the bulk materials for a given polarization in i direction can be calculated through

$$\alpha_{ii}^{\text{bulk}} = \frac{\sqrt{2}\omega}{c} \frac{\text{Im}[\epsilon_{ii}]}{\sqrt{|\epsilon_{ii}| + \text{Re}[\epsilon_{ii}]}} , \quad (4)$$

where ω is the frequency of light, and c is the vacuum speed of light.

The absorption coefficients of bulk Bi_2O_2X are shown in Figs. 2(a)–2(c), indicating the sensitive photoresponse of this group of materials, especially in the high-frequency range. The average absorption coefficients of bulk Bi_2O_2X for visible light are 1.7, 2.4, and $4.5 \times 10^5 \text{ cm}^{-1}$ for $X = \text{S}, \text{Se}$, and Te , respectively. Such values are higher than those of Si and GaAs (5×10^4 and $1 \times 10^5 \text{ cm}^{-1}$, respectively, in sunlight), indicating a high density of light absorption of bulk Bi_2O_2X . As the transmission light intensity decays by $I = I_0 e^{-\alpha d}$ through material layers with a thickness of d , a large proportion (approximately 63%) of visible light can be absorbed through a thickness of $d \sim (1/\alpha) \sim 20 - 60 \text{ nm}$, which makes

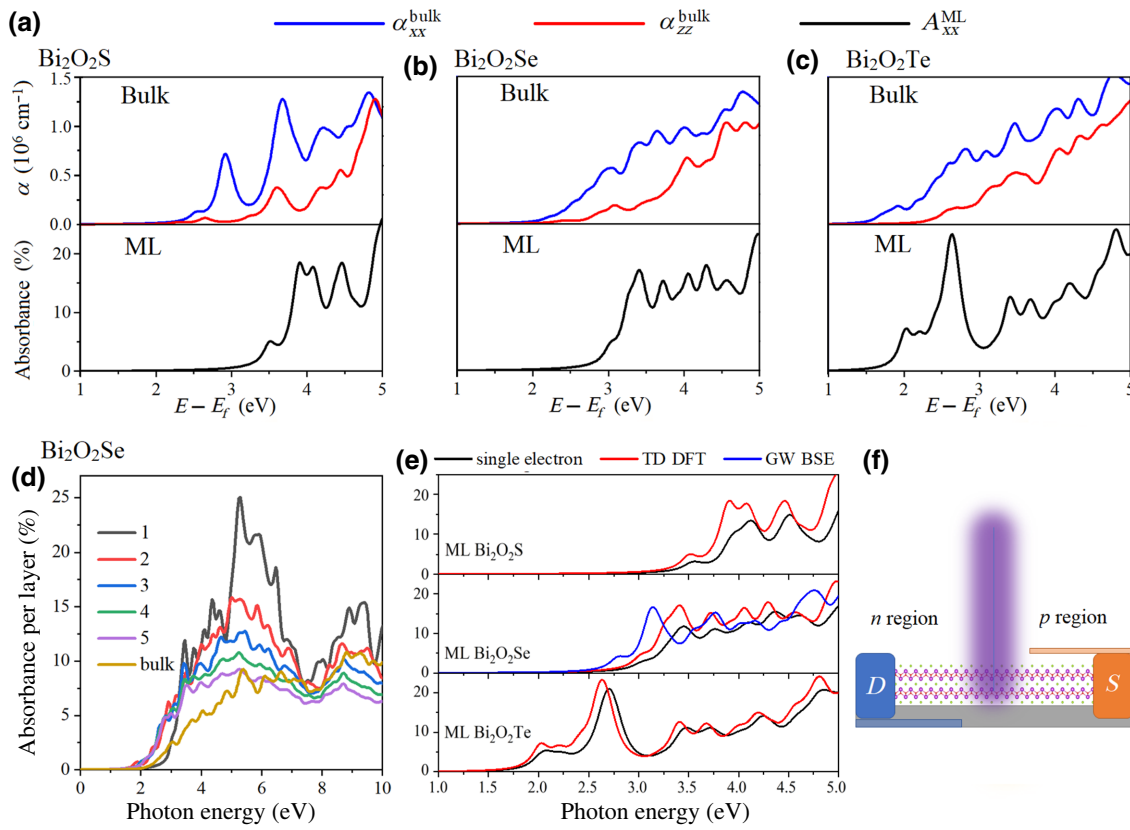


FIG. 2. Optical properties and scaling effect of Bi_2O_2X . (a)–(c) Absorption spectra of incidence light for $\text{Bi}_2\text{O}_2\text{S}$, $\text{Bi}_2\text{O}_2\text{Se}$, and $\text{Bi}_2\text{O}_2\text{Te}$, respectively, calculated by TD DFT method. Red (blue) lines represent absorption coefficient in bulk crystals for photon polarization perpendicular (parallel) to BiO layers, and black lines represent absorbance of light (incident from z direction and polarized to x direction) by ML Bi_2O_2X (in x - y plane). (d) Average absorbance of each layer for 2D $\text{Bi}_2\text{O}_2\text{Se}$ with different layers compared with bulk $\text{Bi}_2\text{O}_2\text{Se}$. (e) Comparison between light absorbance of ML Bi_2O_2X calculated by different methods. Red lines, blue lines, and black lines are calculated by TD DFT, GW BSE, and single-particle approximation, respectively. (f) Illustration of photovoltaic device with 2D Bi_2O_2X contacted by two electrodes.

ultrathin Bi_2O_2X films applicable for sensitive photodetection. As predicted by the band structures, the absorption edge of Bi_2O_2X is lower for heavier X^{2-} ions, and the x - and y -polarized light is under stronger absorption with a lower absorption edge than that of z -polarized light.

The 2D Bi_2O_2X material has layer-dependent optical properties. The absorption coefficients, α_{ML} , of ML Bi_2O_2X are also derived by our TD DFT calculation. The total absorbance of a ML is then computed by $A = \alpha_{\text{ML}}d$, where d is the layer thickness, and the results are shown in Figs. 2(a)–2(c). Remarkably, the absorbance of ML Bi_2O_2X reaches 10%–20% for high-frequency light. Considering the high absorption edges for ML $\text{Bi}_2\text{O}_2\text{S}$ and $\text{Bi}_2\text{O}_2\text{Se}$, their absorption of low-frequency light is limited, but an intense absorption exists for ultraviolet light. As the indirect band gap limits the recombination of electrons and holes and leads to a long carrier lifetime, light absorption creates appreciable amounts of excited carriers that contribute to the transport photocurrent.

The layer-dependent absorbance in 2D $\text{Bi}_2\text{O}_2\text{Se}$ is calculated to investigate the scaling effects, as shown in Fig. 2(d). We calculate the absorbance per layer by $A = \alpha d/n$, where α , d , and n are the absorption coefficients, the total thickness, and the number of the layers, respectively. ML $\text{Bi}_2\text{O}_2\text{Se}$ has a higher absorption edge than that of multilayer films. However, ML $\text{Bi}_2\text{O}_2\text{Se}$ has the largest value of A for high-frequency light. The absorbance is negatively related to the number of layers for $h\nu > 3.2$ eV, indicating high photosensitivity for high-frequency light of few-layer $\text{Bi}_2\text{O}_2\text{Se}$ films. The joint density of states (JDOS) of ML $\text{Bi}_2\text{O}_2\text{Se}$ has steeper steps than the JDOS of multilayer $\text{Bi}_2\text{O}_2\text{Se}$ at the absorption edge due to its 2D nature (see Fig. S3 within the Supplemental Material [40]). The higher JDOS in the high-frequency region leads to a stronger absorption, which explains the layer dependence of Bi_2O_2X photoabsorption. Additionally, the exciton effects are more evident for 2D materials because the screening therein is weaker than that in bulk crystals [43]. The exciton effects can further enhance the absorption of few-layer Bi_2O_2X , especially for low-frequency light [Fig. 2(e)].

In Fig. 2(e), we compare the absorption spectra of ML Bi_2O_2X computed by the TD DFT method and the independent particle approximation. The many-body effects (local exchange correlation and exact exchange) considered in TD DFT with a hybrid kernel make the spectrum shift to a lower-frequency range and generally shift upward. For example, the absorbance of 3.4 eV (the first peak) photons by ML $\text{Bi}_2\text{O}_2\text{Se}$ is 17% and 11%, as determined by TD DFT and the single-particle approximation, respectively. However, the many-body effects are not fully considered in TD DFT, and the GW BSE results show a small additional redshift of the absorption edge compared with the TD DFT results.

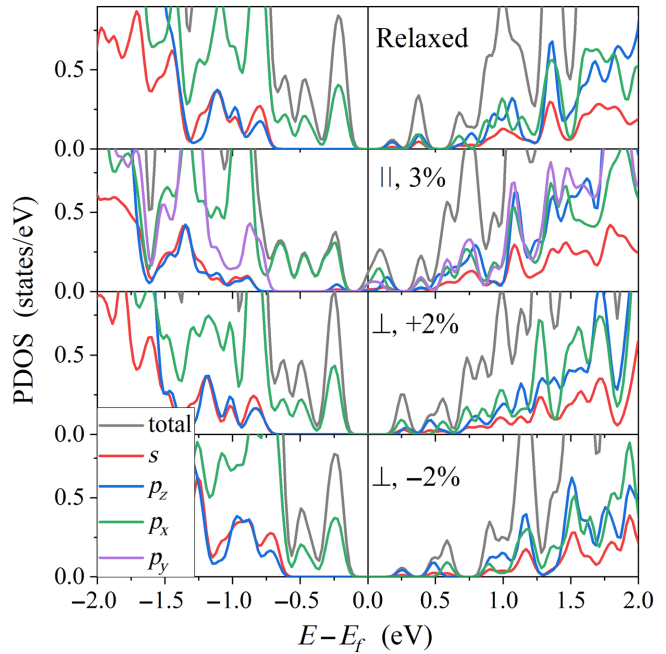


FIG. 3. Electronic structure of bulk $\text{Bi}_2\text{O}_2\text{Te}$ modulated by strain. Partial density of states (PDOS) of fully relaxed crystal, crystal with in-plane anisotropic strain of 3%, vertical expansion of 2%, and vertical compression of 2%. Total density of states and their projections to s , p_x , p_y , and p_z orbitals are plotted as gray, red, green, purple, and blue lines, respectively.

The optical properties of bulk $\text{Bi}_2\text{O}_2\text{Se}$ can be modulated by compression in the vertical or intralayer directions, leading to the transition from the indirect to the direct band gap [38]. Here, we find that the metal-semiconductor transitions appear in $\text{Bi}_2\text{O}_2\text{Te}$ under intralayer anisotropic strain, as shown in Fig. 3. The intralayer anisotropic strain of 3% makes the valence bands strongly overlap with the conduction bands at the Fermi level, providing an effective way to modulate both the electronic and optoelectronic properties. The band gap of about 0.24 eV for bulk $\text{Bi}_2\text{O}_2\text{Te}$ shows robustness under vertical (interlayer) strain in comparison with the sensitive dependence for $\text{Bi}_2\text{O}_2\text{Se}$ [38].

The $\text{Bi}_2\text{O}_2\text{Te}$ band gap is sensitive to intralayer anisotropic strain because of the orbital components of the CBM and VBM. The strain splits the p_x and p_y lines, and compression in the x direction lifts the valence p_x bands at the X point upward to close the band gap. In contrast, vertical strain mainly acts on the conduction bands at the Γ point. The 2% expansion leads to the $p_{x,y}$ -dominant CBM compared with the p_z -dominant CBM under relaxed and compressed conditions, as shown in Fig. 3, because the reduced broadening of the p_z bands through expansion lifts the p_z bands above the $p_{x,y}$ bands. Therefore, one can modulate the selection rule for the direct-band-gap transition by vertical strain.

B. Photovoltaic properties in 2D Bi_2O_2X p - n junctions

To directly examine the performance of Bi_2O_2X in devices, we construct the abrupt-change ML Bi_2O_2X p - n junction (free-standing) with heavy doping of 10^{19} cm^{-3} and calculate the photocurrent. A similar or even higher doping level is commonly applied in 2D-material-based device simulations [13,44,45]. Despite the challenges of heavy doping in Bi_2O_2X , recent experimental progress has made a doping level of 10^{19} cm^{-3} possible. For example, carrier concentrations of 1.83×10^{19} and 10^{19} cm^{-3} have been realized through Ge doping and La doping, respectively [46,47]. Another way to realize the heavy-doping condition is electric doping by contacting the 2D materials with a metal electrode [48,49]. For example, a doping level of $3.1 \times 10^{19} \text{ cm}^{-3}$ in transition metal dichalcogenides (TMDC) is realized by contacting with the Pd electrode [49]. Various other doping strategies for 2D layered materials include ion implantation, plasma treatment, and surface-charge transfer; these strategies realize even higher doping levels of about 10^{14} cm^{-2} [50]. The atomic structure and local density of states (LDOS) of such a ML $\text{Bi}_2\text{O}_2\text{Se}$ p - n junction are shown in Fig. 4(a). A built-in potential is formed in the junction of about 10 nm in length that provides a drifting field for photoexcited carriers. The photoinduced carrier distribution in a p - n junction is illustrated in Fig. 4(b). The carriers drift with the built-in field and then diffuse to form the majority carrier current.

The photovoltaic effects of the zero-bias ML Bi_2O_2X p - n junctions are characterized by (1) the photocurrent density for unit photon flux density [Fig. 5(a)]; (2) the responsivity [Fig. 5(b)], which is defined as the photocurrent for unit power of incident light $R = I/P$; and (3) the external quantum efficiency (EQE) [Fig. 5(c)], which is defined as $E = (I/e\Phi)$, where I is the photocurrent and Φ is the flux of photons. The photocurrents appear from photon energies of 1.1, 1.8, and 2.4 eV and peak at 1.4, 2.3, and 2.9 eV for $X = \text{Te}, \text{Se}$, and S , respectively. The peak responsivity is about 80 mA/W for the ML $\text{Bi}_2\text{O}_2\text{Se}$ p - n junction at zero-bias voltage. Compared with

the peak responsivities of about 40, 45, and 70 meV for the ML WSe_2 , MoS_2 , and BP p - n junctions, respectively [Fig. 5(d)], the ML $\text{Bi}_2\text{O}_2\text{Se}$ p - n junctions show outstanding responsivity. An EQE of up to 18% can be realized in the ML $\text{Bi}_2\text{O}_2\text{Se}$ p - n junctions within our calculations, indicating a reasonably high conversion efficiency.

A larger band gap means a stronger built-in potential, which ensures the efficient collection of carriers by electrodes, but leads to a lower cutoff wavelength of light absorption that limits the effective spectral range. In Fig. 5(b), the ML $\text{Bi}_2\text{O}_2\text{S}$ device has almost zero response to photons under 2.5 eV. In comparison, the overall photocurrent spectra of the ML $\text{Bi}_2\text{O}_2\text{Te}$ device are low due to ineffective current formation caused by the weak built-in field. Therefore, the ML $\text{Bi}_2\text{O}_2\text{Se}$ p - n junction shows the highest responsivity among ML Bi_2O_2X . Despite these limitations, the shortcoming of the ML $\text{Bi}_2\text{O}_2\text{Te}$ device can be overcome by the reverse bias, and the ML $\text{Bi}_2\text{O}_2\text{S}$ device is suitable for interaction with high-frequency light.

As TMDs and group V 2D materials are also recommended for photovoltaic applications [8,51,52], their responsivity is shown in Fig. 5(d) through our device simulations. The ML MoS_2 and WSe_2 p - n junctions display a similar responsivity that rises from $h\nu \simeq 1.6$ eV and peaks at 1.9 eV with a maximum of $R \simeq 40$ mA/W. In comparison, BP and antimonene display a strong photocurrent peak with maximum R values of about 70 and 100 mA/W, respectively. BP and antimonene also have low absorption edges, and the strong absorption peak at 1.3 eV of BP also enables sensitive photodetection to infrared light. As predicted by dielectric calculations in the previous work, our device simulation confirms the potential photoelectric applications of ML antimonene.

To compare the general performance of the 2D materials in terms of photoelectric properties, we calculate the total response coefficients under the AM1.5 standard spectrum of sunlight [Fig. 5(e)]. The ML $\text{Bi}_2\text{O}_2\text{Se}$ and $\text{Bi}_2\text{O}_2\text{Te}$ p - n junctions exhibit responsivities of 16.8 and 13.6 mA/W, respectively, which are higher than those of the ML TMD

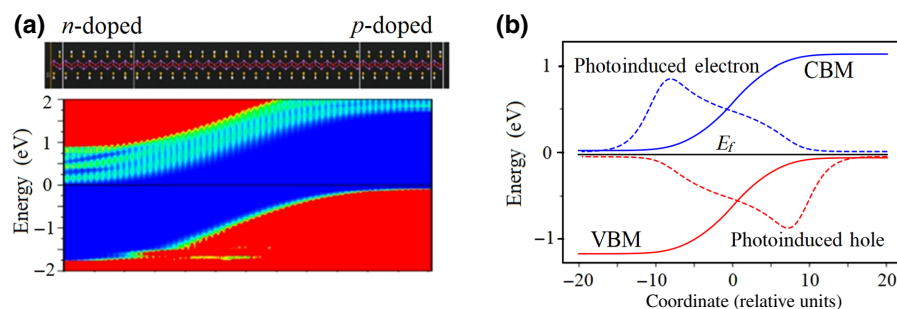


FIG. 4. (a) Device configuration and corresponding LDOS of ML $\text{Bi}_2\text{O}_2\text{Se}$ p - n junction. Color scale from blue to red represents LDOS from low to high. (b) Photoinduced carrier distribution of corresponding slightly doped p - n junction simulated by continuous model. Blue and red solid lines denote CBM and VBM of p - n junction, while blue and red dash lines denote photoinduced electron and hole density, respectively. Fermi level is set as zero.

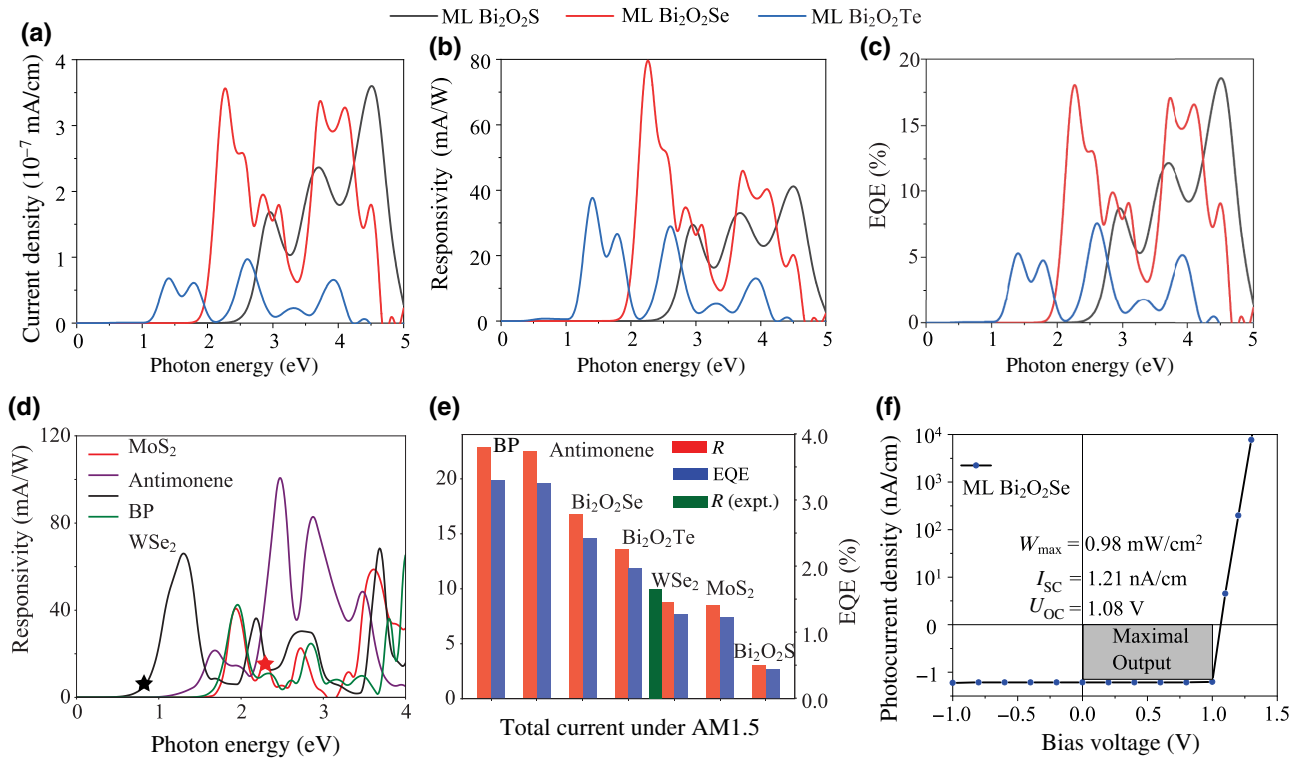


FIG. 5. Photovoltaic properties in ML Bi_2O_2X p - n junctions under different photon energies. (a) Photocurrent density, (b) responsivity, and (c) EQE at $V_{\text{bias}} = 0$ V for photon energies from 0 to 5 eV. (d) Responsivity spectra of ML TMDs (MoS_2 and WSe_2) and group V 2D materials (black phosphorous and antimonene) p - n junctions. Experimental responsivities of ML BP and MoS_2 p - n junctions are denoted by black and red stars, respectively. (e) Comparison of responsivity (red bars) and EQE (blue bars) of calculated ML materials under standard AM1.5 sunlight radiation. Green bar represents experimental data. (f) I - V curve of heavily doped ML $\text{Bi}_2\text{O}_2\text{Se}$ p - n junction under AM1.5 illumination. U_{OC} , I_{SC} , and W_{max} represent open-circuit voltage, short-circuit current, and maximal output power of the device, respectively.

devices, but lower than those of the group V 2D material devices. The group V 2D materials have advantages of low absorption edges, strong interactions with light, and high carrier mobility to achieve high responsivities and conversion efficiencies of the photocurrent. However, black phosphorous is unstable in air [53,54], and antimonene has a band gap that rapidly drops to zero for an increasing numbers of layers [55,56]; these features limit their applications. By contrast, 2D $\text{Bi}_2\text{O}_2\text{Se}$ displays air stability [15,18], band gaps in a moderate range [11], and reasonably high responsivity, and thus, it is applicable for various scales and designs of devices [1,12,17,19]. The I - V curve of the ML $\text{Bi}_2\text{O}_2\text{Se}$ p - n junction is shown in Fig. 5(f), and a very large open-circuit voltage of 1.08 V is obtained. The maximal output power of this p - n junction as a photovoltaic device is $W_{\text{max}} = 0.98 \text{ mW/cm}^2$ under a working voltage of about 1 V. As the total radiation power of AM1.5 solar spectra is $W_{\text{tot}} = 100 \text{ mW/cm}^2$, the ML $\text{Bi}_2\text{O}_2\text{Se}$ p - n junction could reach an energy conversion efficiency of $W_{\text{max}}/W_{\text{tot}} \simeq 1\%$.

The calculated responsivities of three ML 2D p - n junctions are consistent with previous experiments, as shown in Table I. For example, the responsivity of the ML

MoS_2 [24] and BP [23] p - n junctions are measured to be 16.6 and 6.2 mA/W, respectively, for incident light with wavelengths, λ , of 532 and 1550 nm; these values are in agreement with the theoretical values derived from the spectra in Fig. 5(d) of about 18 and 5.7 mA/W, respectively. The ML WSe_2 p - n junction's responsivity is measured to be 10 mA/W under white light and is 8.8 mA/W according to our simulation under AM1.5 illumination [21]. Despite the difference between white light

TABLE I. Comparison of the photoresponsivity of zero-bias ML p - n junctions between our simulation and experiments. λ , R_{calc} , and R_{expt} represent the wavelength of incident light, the calculated responsivity, and the experimental responsivity, respectively. The responsivity of the ML WSe_2 p - n junction is measured under sunlight in the experiment and simulated under AM1.5 illumination in our calculations.

Material	λ (nm)	R_{calc} (mA/W)	$R_{\text{expt.}}$ (mA/W)
ML MoS_2	532	18.0	16.6
ML WSe_2	AM1.5	8.8	10
ML BP	1550	5.7	6.2

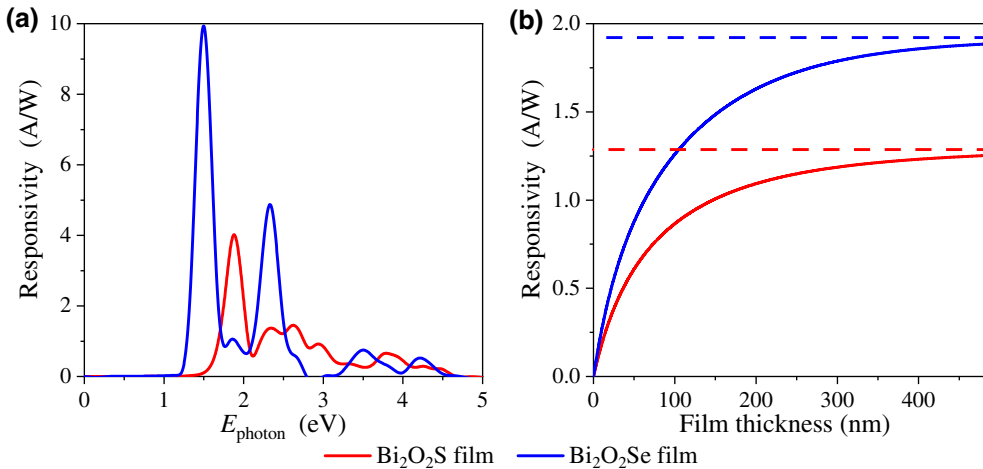


FIG. 6. Photoresponsivity comparison between multilayer $\text{Bi}_2\text{O}_2\text{S}$ and $\text{Bi}_2\text{O}_2\text{Se}$ p - n junctions (a) at thickness of 100 nm for different incident photon energies. (b) Thickness dependence of $\text{Bi}_2\text{O}_2\text{Se}$ and $\text{Bi}_2\text{O}_2\text{S}$ thin film under AM1.5 sunlight radiation. Dashed lines are saturated values for the bulk limit.

and AM1.5 spectrum of sunlight, their frequency ranges are close to each other. The good consistency between the calculated and observed responsivity clearly indicates that our simulation is reliable.

The Bi_2O_2X ($X = \text{S}, \text{Se}$) films with a thickness of $h \gg c$ (c is the lattice constant in the vertical direction) are simulated through the bulk-device calculation combined with a continuum approximation. The decay of light intensity is considered by the absorption coefficient $\alpha(\omega)$, and the total photocurrent is an integral of the current density $j(\omega)$ from the bulk photocurrent calculation:

$$I(\omega) = \Phi_0 \frac{1 - e^{-\alpha(\omega)h}}{\alpha(\omega)} j(\omega),$$

$$\alpha(\omega) = \omega \sqrt{2\mu\{|\epsilon(\omega)| - \text{Re}[\epsilon(\omega)]\}} \quad (5)$$

where Φ_0 is the incident photon flux, ω is the frequency of light, and μ is the magnetic permeability.

The maximum responsivity reaches 4 and 10 A/W for $X = \text{S}$ and Se , respectively, as shown in Fig. 6(a). The $\text{Bi}_2\text{O}_2\text{Se}$ film p - n junction's maximal responsivity appears at a photon energy of around 1.5 eV, indicating a strong photovoltaic effect under near-infrared light. Besides the excellent photovoltaic properties we predict here, the $\text{Bi}_2\text{O}_2\text{Se}$ film photoconductive devices also show high performance for near-infrared photodetection, as reported in a previous experiment [17].

We also calculate the total photocurrent of the $\text{Bi}_2\text{O}_2\text{S}$ and $\text{Bi}_2\text{O}_2\text{Se}$ devices under AM1.5 illumination as a function of thickness, as shown in Fig. 6(b), and the current tends to saturate around a thickness of $h \simeq 300$ nm. The saturated responsivities are 1.3 and 1.9 A/W for $\text{Bi}_2\text{O}_2\text{S}$ and $\text{Bi}_2\text{O}_2\text{Se}$, respectively. Compared with the photovoltaic responsivities of 0.5 and 1.2 A/W for Si and GaAs p - n junctions [22], the Bi_2O_2X film p - n junctions' responsivities are outstanding, showing that they are promising candidates for photodetectors. Compared with the saturated thickness of about 1 μm for the Si device [9], the

saturated thickness of the $\text{Bi}_2\text{O}_2\text{S}$ and $\text{Bi}_2\text{O}_2\text{Se}$ devices is apparently lower due to their higher absorption coefficients.

IV. CONCLUSION

In this work, we study the layer dependence of light absorption of Bi_2O_2X ($X = \text{S}, \text{Se}, \text{Te}$) and photovoltaic effects in the Bi_2O_2X p - n junctions through TD DFT and quantum-transport simulations. We find strong light absorption of Bi_2O_2X , and the absorbance per layer in 2D Bi_2O_2X films increases with a decreasing layer number for high-frequency light. We calculate the photocurrent in 2D Bi_2O_2X p - n junctions via *ab initio* quantum transport simulations. The ML $\text{Bi}_2\text{O}_2\text{Se}$ p - n junction has an outstanding open-circuit voltage of 1.08 V under AM1.5. The ML $\text{Bi}_2\text{O}_2\text{Se}$ and $\text{Bi}_2\text{O}_2\text{Te}$ p - n junctions have responsivities of 16.8 and 13.6 mA/W, respectively; these values are higher than those of ML WSe₂ and MoS₂ p - n junctions. We also develop multiscale methods for multilayer 2D films and derive high responsivities of 1.3 and 1.9 A/W for the $\text{Bi}_2\text{O}_2\text{S}$ and $\text{Bi}_2\text{O}_2\text{Se}$ junctions, respectively, under AM1.5. The $\text{Bi}_2\text{O}_2\text{Se}$ film and $\text{Bi}_2\text{O}_2\text{S}$ p - n junctions have higher responsivities than those of their commercial Si and GaAs counterparts. Therefore, the Bi_2O_2X group materials are promising for photovoltaic applications in p - n junctions and potentially other configurations, such as van der Waals heterojunctions or Schottky junctions.

ACKNOWLEDGMENTS

This work is supported by the National Natural Science Foundation of China (Grants No. 11674005 and No. 91964101), the Ministry of Science and Technology of China [Grant No. 2016YFB0700600 (National Materials Genome Project)], the Open Fund of IPOC (BUPT), the High-Performance Computing Platform of Peking University, and the MatCloud+ High-Throughput Materials Simulation Engine.

- [1] Q. Fu, C. Zhu, X. Zhao, X. Wang, A. Chaturvedi, C. Zhu, X. Wang, Q. Zeng, J. Zhou, F. Liu, B. K. Tay, H. Zhang, S. J. Pennycook, and Z. Liu, Ultrasensitive 2D $\text{Bi}_2\text{O}_2\text{Se}$ phototransistors on silicon substrates, *Adv. Mater.* **31**, e1804945 (2019).
- [2] H. Li, D. A. Strubbe, and J. C. Grossman, Functionalized graphene superlattice as a single-sheet solar cell, *Adv. Funct. Mater.* **25**, 5199 (2015).
- [3] M. P. Marco Bernardi and Jeffrey C. Grossman, Semiconducting monolayer materials as a tunable platform for excitonic solar cells, *ACS Nano* **6**, 10082 (2012).
- [4] M. A. G. David Ginley, And reuben collins solar energy conversion toward 1 terawatt, *MRS Bull.* **33**, 355 (2008).
- [5] B. Radisavljevic, A. Radenovic, J. Brivio, V. Giacometti, and A. Kis, Single-layer MoS_2 transistors, *Nat. Nanotechnol.* **6**, 147 (2011).
- [6] A. K. Geim, Graphene: Status and prospects, *Science* **324**, 1530 (2009).
- [7] M. Long, P. Wang, H. Fang, and W. Hu, Progress, challenges, and opportunities for 2D material based photodetectors, *Adv. Funct. Mater.* **29**, 1803807 (2018).
- [8] M. Bernardi, M. Palummo, and J. C. Grossman, Extraordinary sunlight absorption and one nanometer thick photovoltaics using two-dimensional monolayer materials, *Nano Lett.* **13**, 3664 (2013).
- [9] E. D. Palik, *Handbook of Optical Constants of Solids* (Academic Press, New York, 1998), Vol. 3.
- [10] X. Zhang, Y. Liu, G. Zhang, Y. Wang, H. Zhang, and F. Huang, Thermal decomposition of bismuth oxysulfide from photoelectric $\text{Bi}_2\text{O}_2\text{S}$ to superconducting $\text{Bi}_4\text{O}_4\text{S}_3$, *ACS Appl. Mater. Interfaces* **7**, 4442 (2015).
- [11] C. Chen, *et al.*, Electronic structures and unusually robust bandgap in an ultrahigh-mobility layered oxide semiconductor, $\text{Bi}_2\text{O}_2\text{Se}$, *Sci. Adv.* **4**, eaat8355 (2018).
- [12] J. Yang, R. Quhe, Q. Li, S. Liu, L. Xu, Y. Pan, H. Zhang, X. Zhang, J. Li, J. Yan, B. Shi, H. Pang, L. Xu, Z. Zhang, J. Lu, and J. Yang, Sub 10 nm bilayer $\text{Bi}_2\text{O}_2\text{Se}$ transistors, *Adv. Electron. Mater.* **5**, 1800720 (2019).
- [13] R. Quhe, J. Liu, J. Wu, J. Yang, Y. Wang, Q. Li, T. Li, Y. Guo, J. Yang, H. Peng, M. Lei, and J. Lu, High-performance sub-10 nm monolayer $\text{Bi}_2\text{O}_2\text{Se}$ transistors, *Nanoscale* **11**, 532 (2019).
- [14] M. Liangruksa, Thermoelectric properties of isoelectronically substituted bismuth compounds: A computational study, *Mater. Res. Express.* **4**, 035703 (2017).
- [15] S. D. N. Luu and P. Vaqueiro, Synthesis, characterisation and thermoelectric properties of the oxytelluride $\text{Bi}_2\text{O}_2\text{Te}$, *J. Solid State Chem.* **226**, 219 (2015).
- [16] P. Ruleova, C. Drasar, P. Lostak, C. P. Li, S. Ballikaya, and C. Uher, Thermoelectric properties of $\text{Bi}_2\text{O}_2\text{Se}$, *Mater. Chem. Phys.* **119**, 299 (2010).
- [17] J. Li, Z. Wang, Y. Wen, J. Chu, L. Yin, R. Cheng, L. Lei, P. He, C. Jiang, L. Feng, and J. He, High-performance near-infrared photodetector based on ultrathin $\text{Bi}_2\text{O}_2\text{Se}$ nanosheets, *Adv. Funct. Mater.* **28**, 1706437 (2018).
- [18] J. Wu, H. Yuan, M. Meng, C. Chen, Y. Sun, Z. Chen, W. Dang, C. Tan, Y. Liu, J. Yin, Y. Zhou, S. Huang, H. Q. Xu, Y. Cui, H. Y. Hwang, Z. Liu, Y. Chen, B. Yan, and H. Peng, High electron mobility and quantum oscillations in non-encapsulated ultrathin semiconducting $\text{Bi}_2\text{O}_2\text{Se}$, *Nat. Nanotechnol.* **12**, 530 (2017).
- [19] U. Khan, Y. Luo, L. Tang, C. Teng, J. Liu, B. Liu, and H. M. Cheng, Controlled vapor–solid deposition of millimeter-size single crystal 2D $\text{Bi}_2\text{O}_2\text{Se}$ for high-performance phototransistors, *Adv. Funct. Mater.* **29**, 1807979 (2019).
- [20] J. S. Ross, P. Klement, A. M. Jones, N. J. Ghimire, J. Yan, D. G. Mandrus, T. Taniguchi, K. Watanabe, K. Kitamura, W. Yao, D. H. Cobden, and X. Xu, Electrically tunable excitonic light-emitting diodes based on monolayer WSe_2 p–n junctions, *Nat. Nanotechnol.* **9**, 268 (2014).
- [21] A. Pospischil, M. M. Furchi, and T. Mueller, Solar-energy conversion and light emission in an atomic monolayer p–n diode, *Nat. Nanotechnol.* **9**, 257 (2014).
- [22] M. Buscema, J. O. Island, D. J. Groenendijk, S. I. Blanter, G. A. Steele, H. S. van der Zant, and A. Castellanos-Gomez, Photocurrent generation with two-dimensional van der Waals semiconductors, *Chem. Soc. Rev.* **44**, 3691 (2015).
- [23] Y. Liu, Y. Cai, G. Zhang, Y.-W. Zhang, and K.-W. Ang, Al-doped black phosphorus p–n homojunction diode for high performance photovoltaic, *Adv. Funct. Mater.* **27**, 1604638 (2017).
- [24] Y. Liu, J. Guo, E. Zhu, L. Liao, S.-J. Lee, M. Ding, I. Shakir, V. Gambin, Y. Huang, and X. Duan, Approaching the Schottky–Mott limit in van der Waals metal–semiconductor junctions, *Nature* **557**, 696 (2018).
- [25] J. Heyd, G. E. Scuseria, and M. Ernzerhof, Hybrid functionals based on a screened Coulomb potential, *J. Chem. Phys.* **118**, 8207 (2003).
- [26] D. J. G. Kresse, From ultrasoft pseudopotentials to the projector augmented-wave method, *Phys. Rev. B* **59**, 1758 (1998).
- [27] J. Furthmüller and G. Kresse, Efficient iterative schemes for ab initio total-energy calculations using a plane-wave basis set, *Phys. Rev. B* **54**, 11169 (1996).
- [28] D. J. Chadi, Special points for Brillouin-zone integrations, *Phys. Rev. B* **16**, 1746 (1977).
- [29] S. Grimme, J. Antony, S. Ehrlich, and H. Krieg, A consistent and accurate ab initio parametrization of density functional dispersion correction (DFT-D) for the 94 elements H–Pu, *J. Chem. Phys.* **132**, 154104 (2010).
- [30] M. Gajdoš, K. Hummer, G. Kresse, J. Furthmüller, and F. Bechstedt, Linear optical properties in the projector-augmented wave methodology, *Phys. Rev. B* **73**, 045112 (2006).
- [31] Bethe Salpeter and Casida equations: a first look, https://www.vasp.at/wiki/index.php/BSE_calculations, Jan. 29, 2021.
- [32] S. Botti, A. Schindlmayr, R. D. Sole, and L. Reining, Time-dependent density-functional theory for extended systems, *Rep. Prog. Phys.* **70**, 357 (2007).
- [33] L. R. Giovanni Onida, Angel rubio, electronic excitations: Density-functional versus many-body Green’s-function approaches, *Rev. Mod. Phys.* **74**, 601 (2002).
- [34] S. Albrecht, L. Reining, R. Del Sole, and G. Onida, Ab Initio Calculation of Excitonic Effects in the Optical Spectra of Semiconductors, *Phys. Rev. Lett.* **80**, 4510 (1998).
- [35] M. Rohlfing and S. G. Louie, Electron-Hole Excitations in Semiconductors and Insulators, *Phys. Rev. Lett.* **81**, 2312 (1998).
- [36] M. Brandbyge, Density-functional method for nonequilibrium electron transport, *Phys. Rev. B* **65**, 5401 (2002).

- [37] S. Smidstrup, et al., QuantumATK: An integrated platform of electronic and atomic-scale modelling tools, *J. Phys.: Condens. Matter* **32**, 015901 (2019).
- [38] X. Huang, C.-Y. Niu, J. Zhang, A. Wang, Y. Jia, and Y. Song, Strain-tunable electronic structure, optical response, and high electron mobility of $\text{Bi}_2\text{O}_2\text{Se}$ crystals, *APL Mater.* **7**, 081110 (2019).
- [39] J.-X. Chen, X.-G. Zhao, X.-X. Dong, Z.-L. Lv, and H.-L. Cui, Density functional study of the electronic, elastic and optical properties of $\text{Bi}_2\text{O}_2\text{Te}$, *Z. Naturforsch., A* **75**, 73 (2019).
- [40] See the Supplemental Material at <http://link.aps.org/supplemental/10.1103/PhysRevApplied.15.064037> for a comparison between GW BSE and TD DFT results, electronic structures of ML $\text{Bi}_2\text{O}_2\text{Se}$ with and without H passivation, and an explanation of the layer dependence of absorption coefficients.
- [41] J. Liu, L. Tian, Y. Mou, W. Jia, L. Zhang, and R. Liu, Electronic and mechanical property of high electron mobility semiconductor $\text{Bi}_2\text{O}_2\text{Se}$, *J. Alloys Compd.* **764**, 674 (2018).
- [42] C. Wang, G. Ding, X. Wu, S. Wei, and G. Gao, Electron and phonon transport properties of layered $\text{Bi}_2\text{O}_2\text{Se}$ and $\text{Bi}_2\text{O}_2\text{Te}$ from first-principles calculations, *New J. Phys.* **20**, 123014 (2018).
- [43] K. S. Thygesen, Calculating excitons, plasmons, and quasi-particles in 2D materials and van der Waals heterostructures, *2D Mater.* **4**, 022004 (2017).
- [44] G. Pizzi, M. Gibertini, E. Dib, N. Marzari, G. Iannaccone, and G. Fiori, Performance of arsenene and antimonene double-gate MOSFETs from first principles, *Nat. Commun.* **7**, 12585 (2016).
- [45] L. Liu, Y. Lu, and J. Guo, On monolayer MoS_2 field-effect transistors at the scaling limit, *IEEE Trans. Electron Devices* **60**, 4133 (2013).
- [46] R. Liu, J.-L. Lan, X. Tan, Y.-C. Liu, G.-K. Ren, C. Liu, Z.-F. Zhou, C.-W. Nan, and Y.-H. Lin, Carrier concentration optimization for thermoelectric performance enhancement in n-type $\text{Bi}_2\text{O}_2\text{Se}$, *J. Eur. Ceram. Soc.* **38**, 2742 (2018).
- [47] L. Pan, Z. Zhao, N. Yang, W. Xing, J. Zhang, Y. Liu, C. Chen, D. Li, and Y. Wang, Effects of sulfur substitution for oxygen on the thermoelectric properties of $\text{Bi}_2\text{O}_2\text{Se}$, *J. Eur. Ceram. Soc.* **40**, 5543 (2020).
- [48] A. Pospischil, M. M. Furchi, and T. Mueller, Solar-energy conversion and light emission in an atomic monolayer p–n diode, *Nat. Nanotechnol.* **9**, 257 (2014).
- [49] H. Fang, S. Chuang, T. C. Chang, K. Takei, T. Takahashi, and A. Javey, High-performance single layered WSe_2 p-FETs with chemically doped contacts, *Nano Lett.* **12**, 3788 (2012).
- [50] Y. Zhao, K. Xu, F. Pan, C. Zhou, F. Zhou, and Y. Chai, Doping, contact and interface engineering of two-dimensional layered transition metal dichalcogenides transistors, *Adv. Funct. Mater.* **27**, 1603484 (2017).
- [51] F. Chu, M. Chen, Y. Wang, Y. Xie, B. Liu, Y. Yang, X. An, and Y. Zhang, A highly polarization sensitive antimonene photodetector with a broadband photoresponse and strong anisotropy, *J. Mater. Chem. C* **6**, 2509 (2018).
- [52] S. Li, T. Wang, X. Chen, W. Lu, Y. Xie, and Y. Hu, Self-powered photogalvanic phosphorene photodetectors with high polarization sensitivity and suppressed dark current, *Nanoscale* **10**, 7694 (2018).
- [53] F. Xia, H. Wang, J. C. M. Hwang, A. H. C. Neto, and L. Yang, Black phosphorus and its isoelectronic materials, *Nat. Rev. Phys.* **1**, 306 (2019).
- [54] A. Ziletti, A. Carvalho, D. K. Campbell, D. F. Coker, and A. H. Castro Neto, Oxygen Defects in Phosphorene, *Phys. Rev. Lett.* **114**, 046801 (2015).
- [55] M. Xie, S. Zhang, B. Cai, Y. Gu, X. Liu, E. Kan, and H. Zeng, Van der Waals bilayer antimonene: A promising thermophotovoltaic cell material with 31% energy conversion efficiency, *Nano Energy* **38**, 561 (2017).
- [56] S. Zhang, Z. Yan, Y. Li, Z. Chen, and H. Zeng, Atomically thin arsenene and antimonene: Semimetal-semiconductor and indirect-direct band-gap transitions, *Angew. Chem., Int. Ed. Engl.* **54**, 3112 (2015).